Supplementary Information for: Ultrafast valleytronic logic operations

Francesco Gucci[1], Eduardo B. Molinero[2], Mattia Russo[1], Pablo San-Jose[2], Franco V. A. Camargo[3], Margherita Maiuri[1], Misha Ivanov[4,5,6], Álvaro Jiménez-Galán[2,4], Rui E. F. Silva[2,4], Stefano Dal Conte[1], Giulio Cerullo[1,3]

[1] *Department of Physics, Politecnico di Milano, Piazza Leonardo da Vinci 32, Milano 20133, Italy*
[2] *Instituto de Ciencia de Materiales de Madrid (ICMM), Consejo Superior de Investigaciones Científicas (CSIC), Sor Juana Inés de la Cruz 3, 28049 Madrid, Spain.*
[3] *CNR-IFN, Piazza Leonardo da Vinci 32, Milano 20133, Italy.*
[4] *Max-Born-Institute, Max-Born Strasse 2A, D-12489, Berlin, Germany.*
[5] *Department of Physics, Humboldt Universität zu Berlin, Berlin, Germany.*
[6] *Technion—Israel Institute of Technology, Haifa, Israel.*

1 Temporal characterization of the pulses

In the main text, we demonstrated that valley polarization, and consequently a transient Faraday rotation signal, can be induced using a pair of linearly and perpendicularly polarized pump pulses. This effect persists even when the pulses are fully temporally separated. To verify this, we estimated the temporal duration of the pulses using the polarization-gated frequency resolved optical gating (PG-FROG) [1, 2] technique, which is based on the optically induced birefringence due to the Kerr effect [3], as schematically shown in Fig. S1a.

For the temporal characterization, we set the delay between the two pump replicas to zero ($t_{12} = 0$), obtaining a single pulse, and we set the linear polarization of the probe pulse to 45° degrees with respect to the pump polarization axis. The intense pump pulse is then focused on a thin isotropic material (160 µm thick fused silica plate) inducing a modification of the refractive index proportional to the pulse intensity (i.e. transient optical Kerr effect). The probe goes through two 200-µm-thick broadband crossed polarizers which are placed right before and after the plate. The transient birefringence induced by the pump pulse causes a rotation of the probe pulse's polarization. Such rotation results in a leakage of the probe pulse through the second polarizer only during the temporal overlap between pump and probe pulses. The map in Fig. S1b displays the spectrum of the leakage of the probe light as a function of the delay time τ. By averaging the map along the energy axis, we obtain the time profile $I_{FROG}(\tau)$ shown in Fig. S1c (blue dots). Since PG-FROG is a third-order nonlinear optical technique, $I_{FROG}(\tau)$ is not equal to the cross-correlation of the pulses. However, we can retrieve the intensity profile of the pulses $I(t)$ knowing that:

$$I_{FROG}(\tau) = \int I(t)^2 \, |I(t-\tau)| \, dt \tag{1}$$

We find that the full width at half maximum (FWHM) of $I(t)$ is equal to ~ 17.8 fs. We can now retrieve an estimation of the crosscorrelation between the pulses (orange solid line in Fig. S1c) by applying:

$$I_{CROSS}(\tau) = \int I(t) \, |I(t-\tau)| \, dt \tag{2}$$

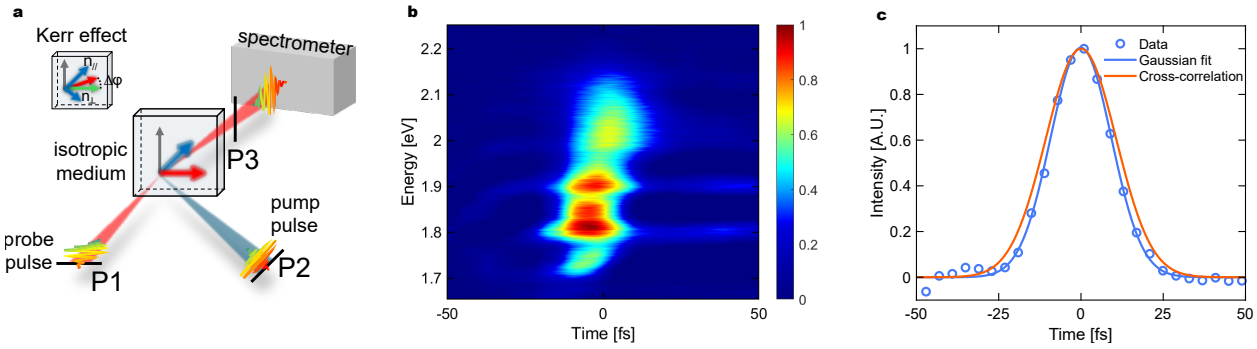

Figure S1: Polarization-gated frequency resolved optical gating (PG-FROG). a, Schematic representation of the technique, with P1, P2, and P3 as polarizers. The sketch in the top left illustrates the Kerr effect, which induces transient birefringence. **b**, Intensity spectrum obtained by scanning the pump-probe delay. **c**, Autocorrelation time trace, derived by averaging the map along the energy axis. The circles represent the experimental data, while the light blue solid line is the Gaussian fit. The orange solid line represents the estimated cross-correlation.

We determine that the FWHM of $I_{CROSS}(\tau)$ is $\sim 25.2 fs$. The cross-correlation reaches the 5% of its initial value after 26.2 fs, and the 1% after 32.5 fs. Therefore, we can safely assume that for $t_{12} > 35 fs$ the pump pulses are completely separated.

2 Static absorption spectrum of WS_2 monolayer

The absorption spectrum of the sample was measured using a spectrophotometer at room temperature and reported in Fig. S2. Three distinct peaks are visible: the ones at approximately 2 eV and 2.4 eV correspond to the A and B excitons [4–6], respectively. The broad peak observed around 2.8 eV is commonly referred to as the C exciton [7] and it is associated to the nesting of the conduction and the valence bands away from the K point [8, 9].

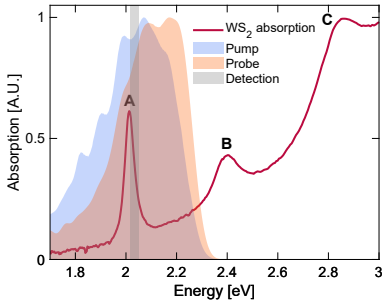

Figure S2: Absorption spectrum and spectra of pump and probe pulses. The solid magenta line represents the absorption spectrum of the WS_2 monolayer, with the A, B, and C excitons labeled. The light blue and orange shaded areas correspond to the spectra of the pump and probe pulses, respectively, while the grey shaded area indicates the detection window.

The pump and probe spectra (shaded areas in Fig. S2) are tuned to be resonant with the A-exciton, avoiding the direct excitation of the B-exciton. After interaction with the sample, a 610±5 nm bandpass filter (corresponding to the energy 2.03 ± 0.017 eV) is used to selectively detect at an energy slightly off-resonant with respect to the A-exciton transition, where the Faraday rotation signal reaches its maximum value [10].

3 Fluence dependent pump-probe measurements

All the measurements shown in the main text were performed in the linear photoexcitation regime. To ensure that we are in this regime, we performed pump-probe measurements as a function of the excitation fluence. For these measurements, t_{12} was set to zero, to have a single pump pulse, and the detection was performed with a spectrometer and a fast CCD camera. Figure S3a shows a typical differential transmission ($\Delta T/T$ map) which is dominated by a positive peak centered at 2.01 eV, associated to a photobleaching of the A-exciton transition [11]. We repeated the same measurements by varying the pump fluence over almost two orders of magnitude spanning from 3.2 $\mu J/cm^2$ to 175 $\mu J/cm^2$. In Fig. S3b, the $\Delta T/T$ spectra for different fluences are displayed.

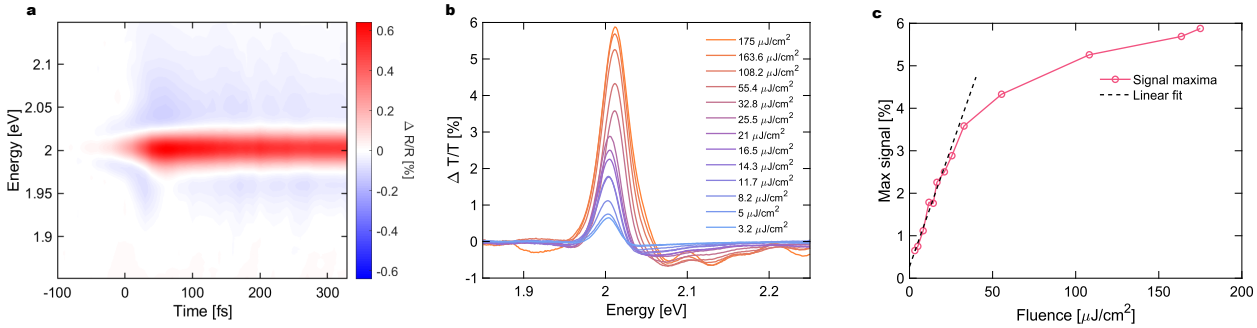

Figure S3: Fluence dependence of pump-probe signal. **a**, $\Delta T/T$ map taken at 3.2 $\mu J/cm^2$. **b**, $\Delta T/T$ spectra measured at the same delay for different pump fluences. **c**, Signal maxima at the different fluences. The circles are data extracted from the $\Delta T/T$ maps, the magenta solid line is a guide for the eye. The dashed line shows that the transient response of the material has a linear behavior up to $\sim$30 $\mu J/cm^2$.

By plotting the maxima of the bleaching signal of the A exciton as a function of the incident fluence, we obtain the curve in Fig. S3c. The threshold for the linear regime is $\sim$30 $\mu J/cm^2$. For this reason, all the measurements reported in the main text were performed with a pump fluence $< 10 \mu J/cm^2$.

4 Two-pulse time-resolved Faraday rotation experiment

In the main text, we show that a sequence of phase-locked few-cycle optical pulses with perpendicular polarization and controlled delay induces a selective valley population in K or K'. The selective population is detected by measuring the rotation of a delayed probe pulse. By scanning the pump-pump delay, t_{12}, with sub-fs precision, the Faraday rotation of the probe displays oscillations, with a period defined by the energy of the A-exciton. Figure S4a shows the Faraday rotation signal measured at different fixed delay times t_{pr} between the pump pairs and the probe as function of t_{12}. As t_{pr} increases, we notice a gradual reduction in the amplitude of the oscillations, while no signal is detected for negative pump-probe delays as expected. The coherent control of the valley polarization on the timescale of the optical cycle can be performed only by timing the two pump replicas characterized by mutual perpendicular polarization. A clear experimental evidence of that is given in Fig. S4b where the same measurement is performed by scanning two linearly polarized pump pulses with parallel polarization (pink line). In this case, the overlap between the excitonic coherence induced by the first pulse in both the valleys and the second pulse leads to homogeneous excitonic excitation in the K and K' valleys.

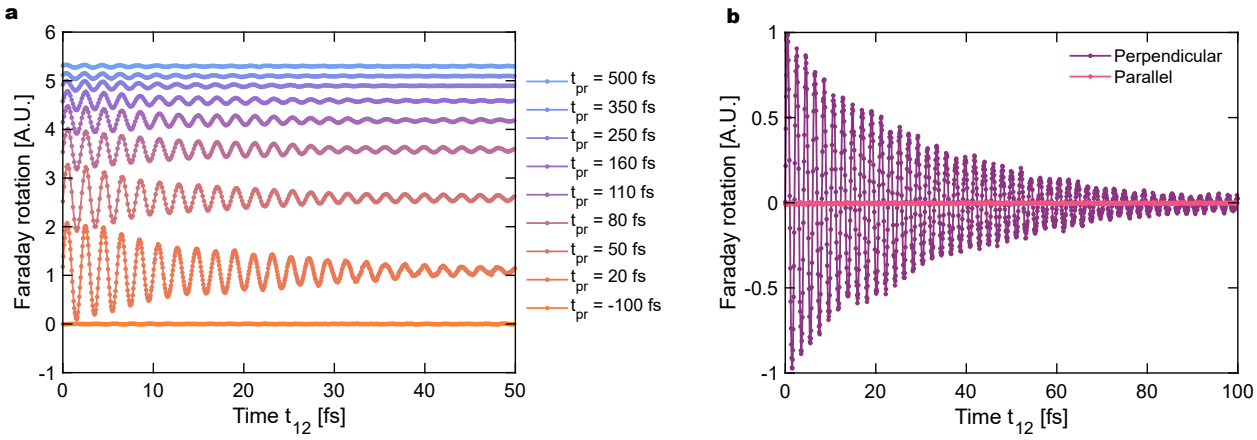

Figure S4: Coherent initialization of the valley index. a, Faraday rotation measurements obtained by scanning the delay t_{12}. The different traces, arranged from the bottom to the top, correspond to gradually increasing pump-probe delays t_{pr}. The dots represent data points, and the solid line serves as a guide for the eye. A vertical offset has been applied to better visualize all the traces. **b**, Comparison of measurements under identical experimental conditions but with different pump polarizations. The purple line indicates the Faraday rotation resulting from perpendicularly polarized pumps, while the pink line corresponds to parallel polarizations.

5 Analytical Model

Within this section we are going to derive analytical expressions, starting from the 3-level model Hamiltonian described in the Method's section. To simplify things, we are going to treat the interaction of the laser field with the target in a perturbative way, only considering the first order term, whose scaling parameter is denoted by α. Furthermore and for the sake of simplicity, we consider the interaction of each pulse to be almost instantaneous. In this way and following the recipe outlined in the Methods section, we can describe the action of the laser pulse in the x direction with the evolution operator,

$$U_x = \begin{pmatrix} 1 & \alpha & \alpha \\ \alpha & 1 & 0 \\ \alpha & 0 & 1 \end{pmatrix}, \tag{3}$$

where $\alpha \ll 1$. In a similar way, the evolution due to a field in the y-direction can expressed as

$$U_y = \begin{pmatrix} 1 & i\alpha & -i\alpha \\ -i\alpha & 1 & 0 \\ i\alpha & 0 & 1 \end{pmatrix} \tag{4}$$

and thus, the optical selection rules are preserved.

The dynamics in the absence of the laser pulse are straightforward,

$$\rho\left(t+\delta t\right) \equiv D_{\delta t}\left[\rho\left(t\right)\right], \tag{5}$$

where $D_{\delta t}$ is a superoperator representing the time evolution. It acts on the density matrix as

$$D_{\delta t}\left[\rho\left(t\right)\right] = \begin{pmatrix} \rho_{gg}\left(t\right) & e^{-\delta t\left(\gamma - i\omega_f\right)}\rho_{g\mathbf{K}}\left(t\right) & e^{-\delta t\left(\gamma - i\omega_f\right)}\rho_{g\mathbf{K}'}\left(t\right) \\ e^{-\delta t\left(\gamma + i\omega_f\right)}\rho_{\mathbf{K}g}\left(t\right) & n(t) + e^{-\delta t 2\gamma_V}P(t) & e^{-\delta t\gamma'}\rho_{\mathbf{K}\mathbf{K}'}\left(t\right) \\ e^{-\delta t\left(\gamma + i\omega_f\right)}\rho_{\mathbf{K}'g}\left(t\right) & e^{-\delta t\gamma'}\rho_{\mathbf{K}'\mathbf{K}}\left(t\right) & n(t) - e^{-\delta t 2\gamma_V}P(t) \end{pmatrix}, \tag{6}$$

where we have defined $n(t) = \frac{1}{2}\left[\rho_{\mathbf{K}\mathbf{K}}\left(t\right) + \rho_{\mathbf{K}'\mathbf{K}'}\left(t\right)\right]$, $P(t) = \frac{1}{2}\left[\rho_{\mathbf{K}\mathbf{K}}\left(t\right) - \rho_{\mathbf{K}'\mathbf{K}'}\left(t\right)\right]$, $\gamma = \gamma_D + \gamma_V/2$ and $\gamma' = \gamma_D + \gamma_V$.

In the two-pulse setup, we have a pulse polarized along x axis at $t = 0$, and another pulse polarized along y axis at $t = t_{12}$. We can approximate the density matrix at times t such that $t_{12} < t$ as

$$\rho\left(t\right) = D_{t-t_{12}}\left[U_y\left(D_{t_{12}}\left[U_x\rho_0 U_x^\dagger\right]\right)U_y^\dagger\right]. \tag{7}$$

It is quite intuitive to grasp what the previous equation means. At first, an instantaneous pulse (U_x) arrives in the x-direction. Afterwards, the system evolves freely ($D_{t_{12}}$), until a second pulse (U_y) arrives in the y-direction. Within this simple approximation and after some algebra, we can write the valley polarization as

$$\rho_{\mathbf{K}\mathbf{K}}\left(t\right) - \rho_{\mathbf{K}'\mathbf{K}'}\left(t\right) = 4\alpha^2 \sin\left(\omega_f t_{12}\right) e^{-t_{12}(\gamma_D + \gamma_V/2)} e^{-2\gamma_V(t-t_{12})}. \tag{8}$$

If we plug into the previous expression the numerical values used in the experiment, we see that we reproduce the shape of the valley polarization, see Fig. S5a. We want to stress out that despite the simplicity of the model, it accurately captures the dynamics of the process.

Now, we can proceed accordingly and obtain analytical expressions by concatenating (appropriately) the action of U_x, U_y and $D_{\delta t}$. We will do this for four different scenarios: only one pulse ($t < t_{12}$),

$$P(t) = 0, \tag{9}$$

two pulses ($t_{12} < t$) in x and y directions respectively,

$$P(t) = 2\alpha^2 e^{-t_{12}\gamma - 2(t-t_{12})\gamma_V} \sin\left(t_{12}\omega_f\right) \tag{10}$$

three pulses ($t_{12} + t_{23} < t$) in x, y and x directions respectively,

$$P(t) = 2\alpha^2 e^{(-\gamma_D t_{13} - \gamma_V(2t - t_{12}))} \left\{ e^{t_{23}\gamma_D + \frac{t_{12}\gamma_V}{2}} \sin\left(t_{12}\omega_f\right) - e^{t_{12}\gamma' + \frac{3t_{23}\gamma_V}{2}} \sin\left(t_{23}\omega_f\right) \right\} \tag{11}$$

and lastly, four pulses ($t_{12} + t_{23} + t_{34} < t$) in x, y, x and y directions respectively.

$$\begin{aligned} P(t) = 2\alpha^2 e^{\left(-\gamma_D t_{13} - \frac{\gamma_V}{2}(4t - 3t_{23} - 3t_{12})\right)} \\ \times \left\{ e^{\frac{1}{2}t_{23}(2\gamma_D - 3\gamma_V)} \sin\left(t_{12}\omega_f\right) - e^{t_{12}\gamma} \sin\left(t_{23}\omega_f\right) + e^{\frac{1}{2}t_{12}(3\gamma_V - 2\gamma_D)} \right\} \\ \times \left\{ e^{(t_{13})\gamma} \sin\left(t_{12}\omega_f\right) + \sin\left(t_{14}\omega_f\right) \right\}, \end{aligned} \tag{12}$$

where we have defined $t_{13} = t_{12} + t_{23}$, $t_{14} = t_{12} + t_{23} + t_{34}$. While the last expression may seem daunting, it can be extremely insightful if we plot it, as shown in Fig. S5b. There, one can appreciate that, again, despite the simplicity of the model it can capture both the amplification and the switching of the valley polarization. This confirms that even though the pulses do not overlap, here they are completely instantaneous, one can still perform operations on the system. Moreover, it further highlights the importance of dephasing in this process, as we stated in the main text.

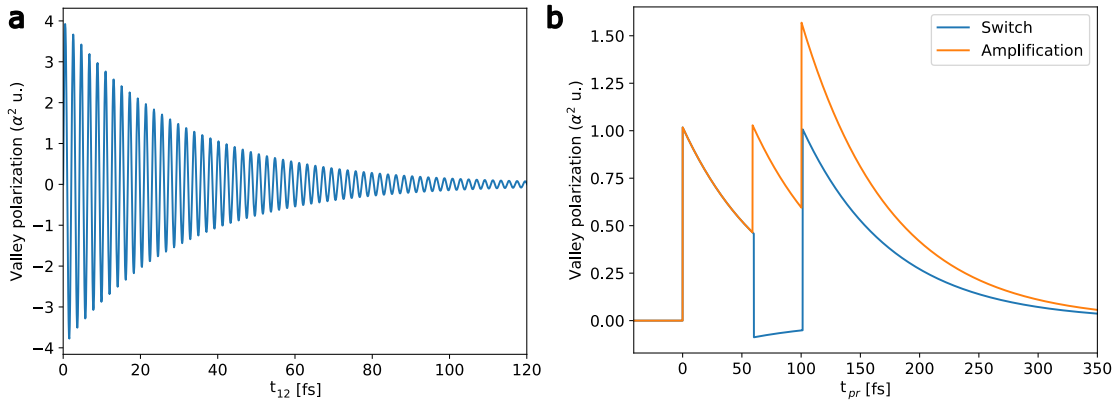

Figure S5: Results from the analytical model. **a**, Valley polarization in the two pulse setup as a funtion of the delay, t_{12} between the two pulses obtained using Eq. 10. **b**, Valley polarization for the four-pulse scenario. The parameters used are $t_{12} = 19.75T_{\text{exc}}$ and $t_{23} = 28.25T_{\text{exc}}$ and $t_{23} = 28.75T_{\text{exc}}$ for the amplification and switching cases, respectively. The curves were obtained using Eq. 12. We have defined $T_{\text{exc}} = 2\pi/E_{\text{exc}}$.

References

[1] Trebino, R. & Kane, D. J. Using phase retrieval to measure the intensity and phase of ultrashort pulses: frequency-resolved optical gating. *JOSA A* **10**, 1101–1111 (1993).

[2] DeLong, K. W., Trebino, R. & Kane, D. J. Comparison of ultrashort-pulse frequency-resolved-optical-gating traces for three common beam geometries. *JOSA B* **11**, 1595–1608 (1994).

[3] Weiner, A. M. *Ultrafast optics* (John Wiley & Sons, 2011).

[4] Mak, K. F., Lee, C., Hone, J., Shan, J. & Heinz, T. F. Atomically thin MoS_2: a new direct-gap semiconductor. *Phys. Rev. Lett.* **105**, 136805 (2010).

[5] Splendiani, A. *et al.* Emerging photoluminescence in monolayer MoS_2. *Nano Lett.* **10**, 1271–1275 (2010).

[6] Ramasubramaniam, A. Large excitonic effects in monolayers of molybdenum and tungsten dichalcogenides. *Phys. Rev. B Condens. Matter* **86**, 115409 (2012).

[7] Li, Y. *et al.* Measurement of the optical dielectric function of monolayer transition-metal dichalcogenides: MoS_2, $MoSe_2$, WS_2, and WSe_2. *Phys. Rev. B* **90**, 205422 (2014).

[8] Carvalho, A., Ribeiro, R. & Castro Neto, A. Band nesting and the optical response of two-dimensional semiconducting transition metal dichalcogenides. *Phys. Rev. B Condens. Matter* **88**, 115205 (2013).

[9] Gillen, R. & Maultzsch, J. Light-matter interactions in two-dimensional transition metal dichalcogenides: Dominant excitonic transitions in mono-and few-layer MoX_2 and band nesting. *IEEE J. Sel. Top. Quantum Electron.* **23**, 219–230 (2016).

[10] Plechinger, G. *et al.* Trion fine structure and coupled spin–valley dynamics in monolayer tungsten disulfide. *Nature Commun.* **7**, 12715 (2016).

[11] Trovatello, C. *et al.* Disentangling many-body effects in the coherent optical response of 2D semiconductors. *Nano Lett.* **22**, 5322–5329 (2022).